
Proceedings Paper:
Vardhan, H., Odavic, M. orcid.org/0000-0002-2104-8893 and Atallah, K. orcid.org/0000-0002-8008-8457 (2022) Design optimization methodology for high-frequency rotary transformers for contactless power transfer systems. In: 2022 IEEE Energy Conversion Congress and Exposition (ECCE). 2022 IEEE Energy Conversion Congress and Exposition (ECCE), 09-13 Oct 2022, Detroit, MI, USA. Institute of Electrical and Electronics Engineers (IEEE) . ISBN 9781728193885

https://doi.org/10.1109/ecce50734.2022.9948210

Design Optimization Methodology for High-Frequency Rotary Transformers for Contactless Power Transfer Systems

Harsha Vardhan
Dept. of Electronic and Electrical Eng.
The University of Sheffield
Sheffield, UK
harshavardhan1@sheffield.ac.uk

Milijana Odavic
Dept. of Electronic and Electrical Eng.
The University of Sheffield
Sheffield, UK
m.odavic@sheffield.ac.uk

Kais Atallah
Dept. of Electronic and Electrical Eng.
The University of Sheffield
Sheffield, UK
k.atallah@sheffield.ac.uk

***Abstract*—This paper describes a novel and all-encompassing optimum design technique for high-frequency radial-type rotary transformers used in contactless power transfer applications. The magnetic, electrical, and thermal properties of the rotary transformer are analytically modelled, and the results are compared to 2-D axis-symmetric FEM simulations. In contrast to the state-of-the-art, which uses standard geometries and assumes important parameters to be constant without investigating their variations and effects, this work employs generic analytical models for design optimization of the radial-type rotary transformer. The transformer is constrained by a given space envelope and a coolant air temperature. This method first determines the significant system parameters, which include the frequency range of 10 kHz to 100 kHz and sets of all realistic system parameters' combinations, which results in the realization of all practical transformer designs, which are then evaluated in terms of loss and mass. This method is used to optimize the design of a 40 kW rotary transformer for a Dual Active Bridge DC-DC converter presented in this paper, highlighting design peculiarities as well as the effect of optimization design factors.**

Keywords—Rotary Transformer, Contactless Power Transfer, Optimization.

I. Introduction

A contactless power transfer (CPT) system based on a rotary transformer (RT) has long been desired, particularly for applications such as spacecraft, electrically excited synchronous machines, and so on [1-2]. RTs outperform brushes and slip rings in terms of reliability and performance. The majority of RT structures in the literature are radial and axial, as shown in Fig. 1a and 1b. However, this study focuses on the radial RT because the manufacturing and mounting tolerances of the ball bearings are significantly smaller in the radial direction than in the axial direction [3], resulting in less air gap and a higher magnetising inductance of the transformer. Furthermore, in the RT literature, the design strategy is quite limited and underemphasized [1], [4-7]. It lacks an understanding of design trade-offs and makes direct decisions based on the applicable optimization approach, without considering the influence of system variables and other factors such as the space envelope. As a result, the goal of this project is to develop an efficient and rapid RT design optimization tool which generates a large number of multi-objective optimized RT designs from which the best candidate can be chosen, minimising both the RT mass and the overall RT loss while meeting the converter requirement.

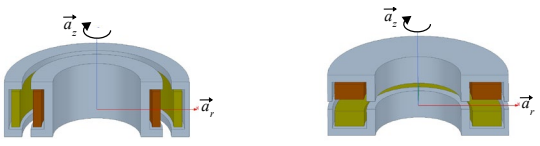

(a) (b)

Fig. 1. Basic configurations of the Rotary Transformer; (a) Radial type and (b) Axial type.

This research looks firstly into the accurate modelling of magnetic, thermal, and electrical aspects of the rotary transformer. Then, a design optimization algorithm is developed including a set of significant system parameters' ranges, which are used to design the shape of the RT while considering space constraints, electrical insulation, air-gap length, and converter requirements. The radial RT mentioned in the study, in particular, is intended for isolated DAB converters with a power rating of 40 kW. The DAB is modulated using the Single-Phase-Shift (SPS) method.

II. Multi-Physics Model of Rotary Transformer and its Validation

RT's magnetic, electric, and thermal properties are represented analytically. The Finite Element Method (FEM) is also used to validate it. These analytical models are used in each iteration of the optimization process. Therefore, accuracy is critical for the models to deliver correct results. Consequently, this section will describe the models of the radial type RT in detail. Fig. 2a depicts all of the symbols used to describe the RT's geometry.

A. Magnetic Model

Using the cylindrical coordinate system (r, φ, z), the radial type RT has been described. Following that, the primary magnetic characteristics of RT, magnetising inductance and leakage inductance, will be determined.

1) Magnetising Reluctance ($\mathfrak{R}_m$) Modelling:

The reluctance network based on the main magnetic flux path, including fringe reluctance, is shown in Fig. 2b. The magnetic circuit is divided into sections where the reluctance of each section is calculated by determining the cross-sectional area and magnetic flux path length of the section. The reluctance of each section's magnetic path is calculated using (1), where S is the cross-sectional area perpendicular to the flux-path length l, dl is an increment, and μ is the medium's permeability, and B & H are magnetic flux density and magnetic field intensity, respectively.

$$\Re = \frac{mmf}{flux} = \frac{\oint \vec{H}.\vec{dl}}{\iint \vec{B}.\vec{dS}} = \int \frac{dl}{\mu S} \tag{1}$$

As shown in Fig. 2b, five different lumped reluctances $\mathfrak{R}_1$, $\mathfrak{R}_2$, $\mathfrak{R}_3$, $\mathfrak{R}_4$, and $\mathfrak{R}'_g$ must be calculated for radial type RT. For example, reluctance $\mathfrak{R}_1$, can be obtained from (1), (2) and (3), with the increment flux path-vector dl taken in the radial direction $\overrightarrow{a_r}$. Reluctance $\mathfrak{R}_1$ is given by (4). Similarly, reluctances $\mathfrak{R}_2$, $\mathfrak{R}_3$, $\mathfrak{R}_4$, and $\mathfrak{R}_g$ can be found and are given by (5)-(8).

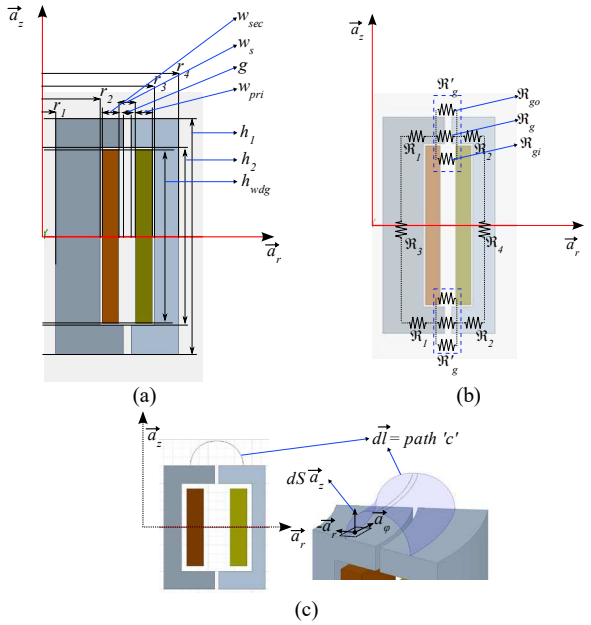

Fig. 2. (a) Side view geometry with secondary inner winding and primary outer winding; (b) Magnetising reluctance network; and (c) Air gap reluctance fringe modelling.

$$\Re_1 = \int_{r=r_i}^{r=r_f} \frac{dr}{\mu\pi(h_1 - h_2)r} \tag{2}$$

$$r_i = \frac{r_1 + r_2}{2}; r_f = \frac{r_2 + r_3 + w_{sec} - w_{pri} - g}{2} \tag{3}$$

$$\Re_1 = \frac{ln\left(\frac{r_2 + r_3 + w_{sec} - w_{pri} - g}{r_1 + r_2}\right)}{\mu\pi(h_1 - h_2)} \tag{4}$$

$$\Re_2 = \frac{ln\left(\frac{r_3 + r_4}{r_2 + r_3 + w_{sec} - w_{pri} + g}\right)}{\mu\pi(h_1 - h_2)} \tag{5}$$

$$\Re_3 = \frac{0.5(h_1 + h_2)}{\mu\pi({r_2}^2 - {r_1}^2)} \tag{6}$$

$$\Re_4 = \frac{0.5(h_1 + h_2)}{\mu\pi({r_4}^2 - {r_3}^2)} \tag{7}$$

$$\Re_g = \frac{ln\left(\frac{r_2 + r_3 + w_{sec} - w_{pri} + g}{r_2 + r_3 + w_{sec} - w_{pri} - g}\right)}{\mu_0\pi(h_1 - h_2)} \tag{8}$$

However, for calculating the shunt fringing reluctances $\Re_{go}$ and $\Re_{gi}$, the basic equation (1) of reluctance can be written as follows. The path 'c' travelled by the fringes, as shown in Fig. 2c will substitute the incremental flux path dl and can be expressed as,

$$c(r, \varphi, z) = g + \pi(r - r_{mean}) = c(r) \tag{9}$$

$$r_{mean} = \frac{\left(r_2 + r_3 + w_{sec} - w_{pri}\right)}{2} \tag{10}$$

Further, to complete the calculation of fringing reluctance, it is necessary to express the elemental surface dS as a function of the integration variables. As shown in Fig. 2c, the flux is fringing out from the elementary surface dS of the core in the $\overrightarrow{a_z}$ and thus can be written as follows.

$$\overrightarrow{dS} = rd\varphi dr\overrightarrow{a_z} \tag{11}$$

Thus, the fringing reluctance can be found by solving the integration presented in the following equation.

$$\Re_{gx} = \left(\int_{r=r_{mean}}^{r=r_{mean}+h_f} \int_{\varphi=0}^{\varphi=2\pi} \frac{\mu_0 r d\varphi dr}{c(r)}\right)^{-1} \tag{12}$$

This integral is performed according to the height of the fringes considered (h_f). This height depends on the geometry and location of the fringes. Thus, referring to Fig. 2b, we have different air gap reluctances for outer and inner paths represented by shunt fringing reluctances $\Re_{go}$ and $\Re_{gi}$, respectively. It is noticed that the fringes outside the structure are much larger than the others. It is therefore a question of defining the height of fringes that are considered for calculations based on accuracy compared to the FEM numerical result. The principle demonstrated for the E-core in [8] is applied here for the radial RT geometry. It is seen that the outer fringes of the outer wall of the transformer will be calculated at a height equal to the half-height of the structure (14). The inner fringes will be considered at a height equal to a minimum of the half-width and half-height of the tooth where the fringes are located (14). Thus, considering all these below is the governing equation to an outer fringing reluctance $\Re_{go}$.

$$\Re_{go} = \frac{1}{2\pi\mu_0\left\{\frac{h_{fouter}}{\pi} + \left(\frac{-g + \pi r_{mean}}{\pi^2}\right) ln\left(\frac{g + \pi h_{fouter}}{g}\right)\right\}} \tag{13}$$

Similarly inner $\Re_{gi}$ is this the same but with a different fringe height (h_{finner}).The h_{fouter} and h_{finner} can be found as

$$\begin{aligned} h_{fouter} &= r_4 - r_{mean} + 0.5g \\ h_{finner} &= min\{(r_3 - r_{mean} + 0.5g), 0.5h_2\} \end{aligned} \tag{14}$$

Thus, the net reluctance across the air gap $\Re_g{}'$ will be equal to the parallel combination of $\Re_{go}$, $\Re_{gi}$ and $\Re_g$. Once we find the reluctance of all sections covering the main flux path, the magnetising reluctance can be calculated by following.

$$\Re_m = 2\left(\Re_1 + \Re_2 + \Re_g{}'\right) + \Re_3 + \Re_4 \tag{15}$$

From this the magnetising inductance L_m referred to the primary side, is given by (16) for radial type, where N_P is the number of turns on the primary winding.

$$L_m = \frac{{N_P}^2}{\Re_m} \tag{16}$$

Fig. 3 shows the validation of the analytical magnetising inductance model with/without including fringing reluctance vs FEM model. Several structures with varying air gaps were evaluated and the accuracy was found to be greater than 90%. (for the air gap, $g = 0.1$ to $1\ mm$) when fringing reluctance is included in the analytical model.

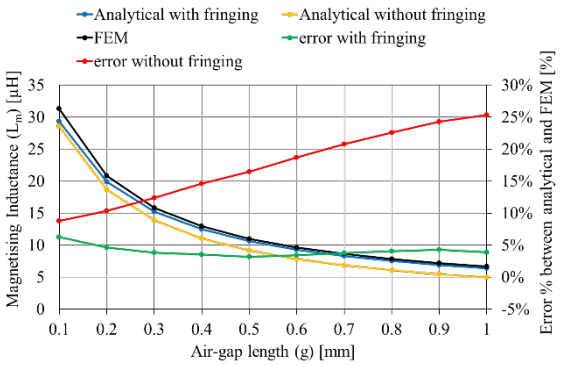

Fig. 3. Magnetising inductance against air gap length: FEM results versus analytical calculation with and without fringing.

2) Leakage Reluctance ($\mathfrak{R}_{lk}$) Modelling:

The magnetic flux which links one winding but not the other contributes to the leakage inductance. To determine this, equal and opposite ampere-turns in the primary and secondary windings, i.e., $N_P I_P = N_S I_S$ are assumed to exclude the effect of magnetising inductance. Thus, under these conditions, the leakage inductance can be calculated analytically by integrating the magnetic energy density over the volume of the transformer's winding window (V_W) as follows:

$$\frac{1}{2} L_{lk} (I_P)^2 = \frac{1}{2} \iiint_{V_W} (\mu_0 H^2)\, dV \tag{17}$$

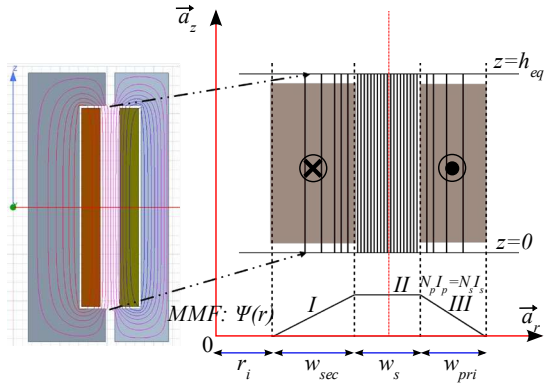

Fig. 4. Leakage field pattern and MMF diagram for Radial type RT.

A leakage field pattern for the radial type RT is shown in Fig. 4, obtained by FEM analysis where primary and secondary ampere-turns have been made equal and opposite. The following assumptions are made for the leakage inductance calculation:

- The core has large permeability thus the MMF induced in the core by this flux is negligible.
- The current density vector is evenly distributed through winding and perpendicular to the cut surface.
- The leakage field is assumed to be axial for the complete window height of the transformer as shown in Fig. 4.

The leakage field pattern can be approximated by a set of parallel flux lines of equal height denoted by h_{eq} in Fig. 4. Considering these equal and opposite ampere-turns, the MMF distribution across the cross-section of the primary and secondary windings is trapezoidal as shown in Fig. 4, where regions I, II and III can be identified and the corresponding MMF given by the following equations for different regions.

$$\begin{aligned} \Psi(r) &= \frac{N_P I_P}{w_{sec}} (r - r_i) && \text{: Region I} \\ \Psi(r) &= N_P I_P && \text{: Region II} \\ \Psi(r) &= \frac{N_P I_P}{w_{sec}} (-r + r_i + w_{sec} + w_s + w_{pri}) && \text{: Region III} \end{aligned} \tag{18}$$

Here, the initial radius r_i (as shown in Fig. 4) can be calculated as

$$r_i = r_{mean} - 0.5 w_s - w_{sec} \tag{19}$$

Thus, the total leakage inductance L_{lk} referred to the primary side is given by (20).

$$L_{lk} = \frac{\mu_0}{(I_P)^2 (h_{eq})^2} \iiint (\psi(r))^2 r d\varphi dz dr \tag{20}$$

Afterwards using the equation of MMF over different regions, we can derive the respective leakage inductance referred to the primary side of radial type RT as (21). The total leakage reluctance ($\mathfrak{R}_{lk}$) is then given by (22).

$$\begin{aligned} L_{lk} = \frac{2\pi\mu_0 N_P^2}{h_{eq}} \Big\{ & \frac{w_{pri}}{3} \left(\frac{w_{pri}}{4} + r_i + w_{sec} + w_s \right) \\ & + w_s \left(r_i + w_{sec} + \frac{w_s}{2} \right) \\ & + \frac{w_{sec}}{3} \left(\frac{3 w_{sec}}{4} + r_i \right) \Big\} \end{aligned} \tag{21}$$

$$\frac{1}{\mathfrak{R}_{lk}} = \frac{L_{lk}}{{N_P}^2} \tag{22}$$

Moreover, to split the leakage reluctance between the primary and secondary, which will be used in electric circuit representation in the next section, the space between the windings i.e. region II is split in half and the integration given in (20) is performed. Thus respective leakage reluctance of the primary and secondary will be given by $(\mathfrak{R}_{lk\_pri})$ and $(\mathfrak{R}_{lk\_sec})$ as following.

$$\begin{aligned} \frac{1}{\mathfrak{R}_{lk\_pri}} = \frac{2\pi\mu_0 N_P^2}{h_{eq}} \Big\{ & \frac{w_{pri}}{3} \left(\frac{w_{pri}}{4} + r_i + w_{sec} + w_s \right) \\ & + w_s \left(\frac{r_i}{2} + \frac{w_{sec}}{2} + \frac{3 w_s}{8} \right) \Big\} \end{aligned} \tag{23}$$

$$\frac{1}{\mathfrak{R}_{lk\_sec}} = \frac{2\pi\mu_0 N_P^2}{h_{eq}} \left\{ \frac{w_{sec}}{3} \left(\frac{3 w_{sec}}{4} + r_i \right) + w_s \left(\frac{r_i}{2} + \frac{w_{sec}}{2} + \frac{w_s}{8} \right) \right\} \tag{24}$$

From (22), (23) and (24), we can also relate the net leakage reluctance as given.

$$\frac{1}{\mathfrak{R}_{lk}} = \frac{1}{\mathfrak{R}_{lk\_pri}} + \frac{1}{\mathfrak{R}_{lk\_sec}} \tag{25}$$

From this, the leakage inductance referred to the primary side and secondary side i.e. L_{lk_pri} and L_{lk_sec}, is given by (26) and (27), where N_P and N_S are the number of turns on the primary and secondary winding respectively.

$$L_{lk\_pri} = \frac{{N_P}^2}{\mathfrak{R}_{lk\_pri}} \tag{26}$$

$$L_{lk\_sec} = \frac{{N_s}^2}{\mathfrak{R}_{lk\_sec}} \tag{27}$$

For completeness, the analytical model of leakage inductance of radial RT available in the literature [1]-[7], calculated under the assumption that the average radius of winding location is relatively greater than the winding window width i.e. $r_{avg} \gg (w_{pri}, w_s, w_{sec})$, is included in this section and is given by (28) and (29). The proposed model given by (26) and (27) is compared against the existing model (28), (29) and the FEM model. From Fig. 5, the accuracy of the proposed model is above 95 % for w_s in the range [0.2,3]. Fig. 5 shows the validation of the analytical primary leakage inductance vs. the FEM model. This is one of the cases where r_{avg} is taken comparable to winding window width which is a standard pot core geometry (P66/56).

$$L_{lk\_pri} = \frac{2\pi\mu_0 N_P^2 r_{avgP}}{h_{eq}} \left\{ \frac{w_{pri}}{3} + \frac{w_s}{2} \right\} \tag{28}$$

$$L_{lk\_sec} = \frac{2\pi\mu_0 N_s^2 r_{avgS}}{h_{eq}} \left\{ \frac{w_{sec}}{3} + \frac{w_s}{2} \right\} \tag{29}$$

$$\begin{aligned} r_{avgP} &= r_{mean} + 0.5(w_s + w_{pri}) \\ r_{avgS} &= r_{mean} - 0.5(w_s + w_{sec}) \end{aligned} \tag{30}$$

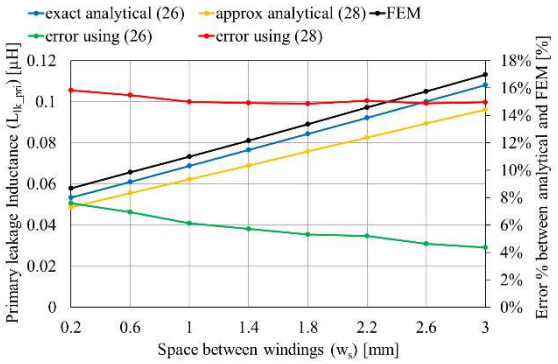

Fig. 5. Primary leakage inductance against air gap length: FEM results versus analytical calculation with exact (26) and approximate (28) equations.

B. Electric Model

1) Transformer model:

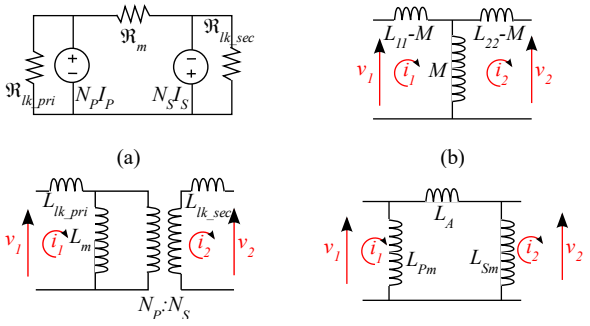

Fig. 6. (a) Magnetic circuit; (b) T-Type electric circuit; (c) Most common electric circuit representation; and (d) π-Type electric circuit; of two-winding rotary transformer.

Fig. 6a shows the standard equivalent magnetic circuit of a two-winding conventional transformer. RT with two windings can be represented by the same magnetic circuit, where $\Re_m$ represents the main flux path reluctance which is presented in Section II-A1, $\Re_{lk\_pri}$ and $\Re_{lk\_sec}$ represents the leakage path reluctance from Section II-A2. The inductance matrix can be obtained as specified in (31), by solving the terminal equations from the given magnetic circuit. This inductance matrix depends on the number of turns and respected reluctance.

$$[L] = \begin{bmatrix} L_{11} & M \\ M & L_{22} \end{bmatrix} = \begin{bmatrix} N_P^2\left(\frac{1}{\Re_{lk\_pri}}+\frac{1}{\Re_m}\right) & \frac{N_P N_S}{\Re_m} \\ \frac{N_P N_S}{\Re_m} & N_S^2\left(\frac{1}{\Re_{lk\_sec}}+\frac{1}{\Re_m}\right) \end{bmatrix} \quad (31)$$

This inductance matrix is the link between the magnetic circuit and electric circuit representation. From (31), all other forms of electric circuits depicted in Fig. 6 can be obtained and are interrelated as (32). The π-type representation will be used in the next section to derive the power flow equation in the DAB converter.

$$\begin{bmatrix} L_{11} & M \\ M & L_{22} \end{bmatrix} = \begin{bmatrix} L_{lk\_pri}+L_m & \frac{N_S}{N_P}L_m \\ \frac{N_S}{N_P}L_m & L_{lk\_sec}+\frac{N_S^2}{N_P^2}L_m \end{bmatrix} \quad (32)$$

2) Core and Litz wire loss model:

To keep the transformer size small, the core of RT is chosen to function at high frequencies; hence, specialised power ferrites (Mn-Zn) with high saturation and low loss are preferable. For calculating the core loss per unit volume, the general Steinmetz equation (GSE) is frequently used under sinusoidal excitation given as (33), however, for applications such as DAB, the core loss in the transformer is calculated using the improved GSE (iGSE) equation (34) [9]. Here k, α, β are Steinmetz coefficients and B_{max} & f are operating maximum flux density and fundamental frequency ($T = 1/f$).

$$P_{GSE} = k f^{\alpha} B_{max}^{\beta} \quad (33)$$

$$P_{iGSE} = k_i \left[\frac{1}{T}\int_0^T \left|\frac{dB}{dt}\right|^{\alpha} (\Delta B)^{\beta-\alpha} dt\right] \quad (34)$$

$$\Delta B = 2B_{max};\ \ k_i = \frac{k}{(2\pi)^{\alpha-1} 2^{\beta-1}\left(\int_0^{2\pi}|cos\theta|^{\alpha}\, d\theta\right)} \quad (35)$$

In the design of high-frequency transformers, eddy-current effects in windings play an important role. Two of these effects are skin-depth and proximity-effect losses. The restrictions of skin depth and proximity effects are addressed by using stranded wire with each strand insulated. Each strand is transposed down the length of the wire to take the place of all the other strands in the cross-section. This guarantees that the magnetic field is uniformly distributed across all strands. As a result, Litz wire can be utilised for this application. Because of the wide design space of the strand number and diameter, and the risk of incurring a very high loss if these parameters are not properly set, it is critical to optimise a Litz wire design. Dowell's model (a hyperbolic-function-based model) is suggested since it is as accurate as the other models [10]. Hence, an expression for the effective winding AC resistance in the case of non-sinusoidal current waveform $i(t)$ is used which is given as (36).

$$\frac{R_{ac}}{R_{dc}} = 1 + \left(\frac{(5p^2-1)}{45}\Delta^4\right)\left(\frac{\left|\frac{d}{dt}i(t)\right|_{rms}}{2\pi f_{sw} I_{rms}}\right)^2 \quad (36)$$

where p is the effective number of layers created by the Litz wire winding and Δ is the penetration ratio, and R_{ac} is the total effective resistance caused by the eddy loss including the loss due to DC resistance R_{dc} as well, given by (38). Using this, the winding loss can be expressed by the following equation.

$$P_{wdg.loss} = {I_{rms}}^2 R_{ac} \quad (37)$$

$$R_{dc} = \frac{4\rho N(MLT)}{\pi N_{str} d_{str}^2} \quad (38)$$

3) Dual Active Bridge (DAB) converter model:

The optimal design of a 40 kW rotary transformer based on the Dual Active Bridge (DAB) converter parameters shown in Table I with a Single-Phase-Shift (SPS) modulation technique is considered in this work. Fig. 7 presents a basic DAB topology incorporating RT and the equivalent π-type electric circuit of RT which is used to carry the further analysis. The power flow equation depends on the modulation technique used. For the given DAB converter, there are several modulation techniques. Note, in general, there are three degrees of freedom: d_P, d_S, and δ, where d_P and d_S are

the duty cycle for the primary and secondary side H-bridges respectively, and δ is the phase shift between the two. To obtain the maximum power flow a duty cycle of 50 % is chosen. Fig. 8 shows the primary current and pole voltages waveforms with SPS modulation, for a given switching frequency $f = f_{sw}$ and $T = T_s = 1/f_{sw}$.

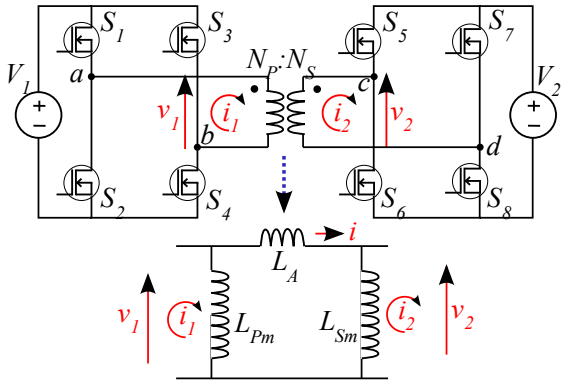

Fig. 7. DAB converter with RT.

TABLE I: DAB CONVERTER SPECIFICATION

Parameter	Symbol	Value
Output Power	P_{out}	40 kW
Input/ Primary side DC Voltage	$V_1 = V_{dc}$	800 V
Output/ Secondary side DC Voltage	$V_2 = V_{dc}$	800 V
Turns Ratio	$N_P : N_S$	1:1
Primary and Secondary Duty cycle	$d_P = d_S$	50 %

The analysis of the transformer is based on the inductance because the resistance is small at the high frequency of DAB operation. Thus power flow equation and converter operation can be analysed by taking the inductance network only as shown in Fig. 7. Equation (39) is the total power transferred and it can be found by averaging the product of instantaneous inductor current $i(t)$ and pole voltage $v_1(t)$.

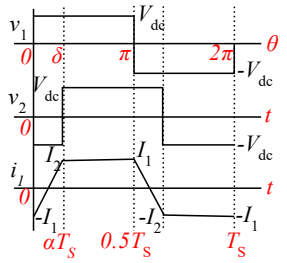

Fig. 8. DAB pole voltages and primary current waveforms.

$$P_{out} = f_{sw}\int_0^{T_s} i(t)v_1(t)dt = \frac{V_1V_2}{2\pi f_{sw}L_A}\left(\delta\left(1-\frac{\delta}{\pi}\right)\right) \tag{39}$$

L_A is the inter-link inductance between the two full bridges and determines the active power flow. Transforming the T-type electric network (Fig. 6b) to π-type (Fig. 6d), L_A can be found as follows, where k is the coupling coefficient.

$$L_A = M\left(\frac{1}{k^2}-1\right);\ k = \frac{M}{\sqrt{L_{11}L_{22}}} \tag{40}$$

Now, to build the RT optimally for the converter's specifications (given in Table I), the phase-shift angle for the given output power needs to be determined and is dependent on the inductances defined by the RT geometry. Equation (41) determines the respective phase-shift angle.

$$\delta = \frac{\pi}{2}\left[1-\sqrt{1-\left(\frac{8f_{sw}L_AP_{out}}{V_1V_2}\right)}\right] \tag{41}$$

Furthermore, it is found that if the primary and secondary side voltages are equal, Zero Voltage Switching (ZVS) will operate under all load conditions up to the maximum power capability [11]. Consequently, switching loss is minimized for the unity turn ratio. As a result, $N_P = N_S$, which equalises primary and secondary side currents, $i_1(t) = i_2(t) \sim i(t)$. For high magnetising inductances, the shape of primary and secondary currents can be approximated by the current flowing through inductance L_A which is trapezoidal. Thus, the governing equations for RMS current can be calculated as follows, which are used in the calculation of winding losses (37).

$$I_{1rms} = I_{2rms} \sim I_{rms} = I_{pk}\sqrt{1-\frac{4}{3}\alpha} \tag{42}$$

$$I_{pk} = \alpha\frac{V_{dc}}{f_{sw}L_A};\ \text{Here, } \alpha = \frac{\delta}{2\pi} \tag{43}$$

$$\left\langle\frac{d}{dt}i(t)\right\rangle_{rms} = \left(2\sqrt{\frac{2}{\alpha}}\right)I_{pk}f_{sw} \tag{44}$$

C. Thermal Model

The surface area, cooling environment, and total losses all influence temperature rise within a transformer. As a result, thermal modelling is an important design feature. The lumped thermal equivalent circuit of the RT is investigated and developed using [4], as illustrated in Fig. 9.

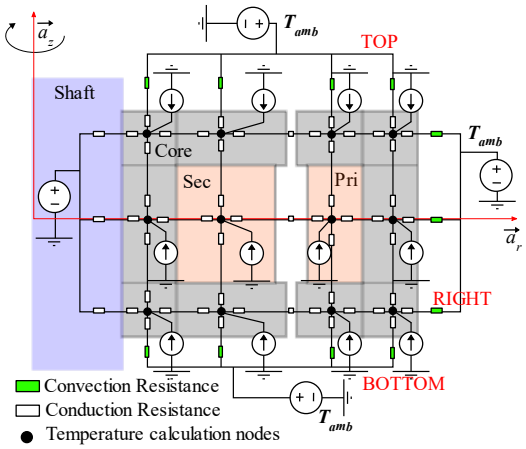

Fig. 9. Steady-state thermal equivalent circuit of radial type RT.

It calculates temperatures at various nodes of the core and windings, which should be limited by the RT's maximum temperature withstanding potential. The lumped steady-state thermal model is created by splitting the transformer core into ten distinct sections while treating the windings as a single unit, as illustrated in Fig. 9. This model considers heat transfer in both the axial and radial directions. As shown in the figure, twelve major nodes are defined and calculated during the optimization process for various RT geometries and losses. The voltage source reflects the temperature in the section, while the current source represents the power loss in the corresponding sections. Conduction thermal resistances are used to simulate heat transfer within a section, whereas convection thermal resistances are used to model heat transfer between a section and the surrounding air. The conduction thermal resistance in $\vec{a_r}$ and $\vec{a_z}$ direction is calculated as follows.

$$R_{th_r} = \frac{1}{2\pi k \Delta z} ln\left(\frac{r_o}{r_i}\right) \quad (45)$$

$$R_{th_z} = \frac{\Delta z}{\pi(r_o^2 - r_i^2)k} \quad (46)$$

Here, Δz represents the length of the section between two nodes where heat is flowing in $\overrightarrow{a_z}$ direction and r_o & r_i represents the outer and inner radius for the respective section thermal calculation. The k is the thermal conductivity and taken equal to 4, 2, and 0.024 $W/(m°C)$ for ferrite core, Litz wire winding and air gap respectively. However, heat transfer to the shaft from the RT is considered negligible for this work. Furthermore, the convection thermal resistance R_{th_x} for the section is calculated using (47), where h is the heat transfer coefficient and A is the cross-section area of the respective section. The h is set to 100, 8, and 8 $W/(m^2°C)$, respectively, for the top, bottom, and right surrounding of RT (Fig. 9). These values are taken from [4] and based on the cooling environment existing in the relevant section, where the predominant airflow is on the top side and the other sides are obstructed by mechanical fixtures.

$$R_{th_x} = \frac{1}{hA} \quad (47)$$

This results in the completion of all the RT multi-physics models utilised in the optimization, and the subsequent section of the paper describes the optimization algorithm.

III. Design Optimization Approach and Discussion

For high-frequency radial-type rotary transformers, this research describes a new and comprehensive optimum design technique.

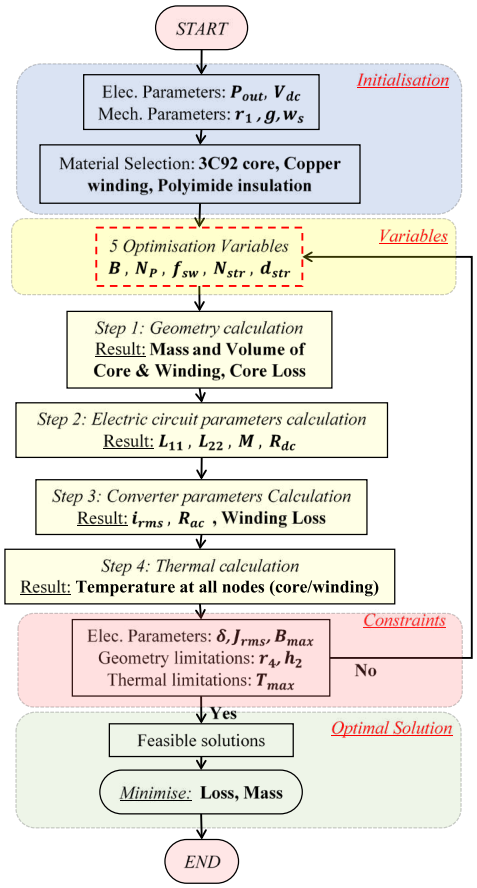

Fig. 10. Optimization flow chart.

Fig. 10 depicts the optimal flow chart proposed in this paper. This method is used to optimize the design of a 40 kW rotary transformer of a Dual Active Bridge (DAB) DC-DC converter, highlighting design peculiarities as well as the effect of different optimization variables.

A. Initialisation

The design process starts with the definition of RT specifications as listed in Table I. In this stage, general initial electrical and mechanical specifications, including output power, voltage, shaft radius, and air gap length, are required. It has been found that the air gap length directly impacts the system performance, so it is fixed to the minimum value possible (Table II) for this application considering ball-bearing tolerances and speed of rotation. In this work the turn ratio (Table I) is defined from the beginning of the optimization process, however, it can also be considered as an optimization variable if required.

B. Variables and Stepwise design process

Initial variables such as shaft radius r_1, transformer width h_1, airgap length g and space between windings w_s are used to construct the transformer. Table II contains the values of the initial variables that are used in the work.

Table II: Initial Variables

Parameter	Symbol	Value
Shaft Radius	r_1	270 mm
RT width	h_1	35 mm
Air-gap length	g	1 mm
Space between windings	w_s	3 mm
Insulation thickness between windings	t_i	40 μm
Insulation thickness between core and winding	t_b	1 mm

Fig. 2a shows all the parameters that are employed. The cross-sectional area (A_c) of RT's main flux path should be designed equally to ensure uniform flux distribution throughout the core. The main governing equation is given by (48).

$$N_P f_{sw} A_c B = \frac{V_{dc}}{4} \quad (48)$$

Based on (48), the design procedure identifies the following optimization parameters, namely N_P, f_{sw} and B. Further, the winding window specifications are required, as it plays an equal and vital part in achieving the optimal mass and loss. Therefore, Litz wire parameters, N_{str} and d_{str} are also treated as the Optimization Variable (OV). The operating range for the identified five optimisation parameters can be found in Table III. Knowing this, the design process begins, consisting of four analytical calculation steps described next in this section.

Step 1. Geometry calculation: From (48), cross-sectional area A_c can be calculated and thus the dimensions r_2 and h_2 can be obtained by,

$$r_2 = \sqrt{\left(\frac{A_c}{\pi} + r_1^2\right)}\ ; \text{and, } h_2 = h_1 - \frac{A_c}{\pi r_1} \quad (49)$$

TABLE III: OPTIMIZATION VARIABLES RANGES FOR RT GEOMETRY DESIGN

Optimization Variable (OV)	Symbol	Min	Max	Units
Operating Flux density	B	0.05	0.2	T
No. of Primary Turns	N_P	2	15	_
Switching Frequency	f_{sw}	10	100	kHz
No. of Strands in Litz wire	N_{str}	1000	4000	_
Diameter of each strand	d_{str}	0.05	0.3	mm

The Litz wire parameters N_{str} and d_{str}, as well as the insulation requirement based on the operating temperature class and breakdown voltage, are further required. Considering the operating temperature (200 ℃) and breakdown voltage ($>$ 3 kV RMS), each copper strand of Litz wires is enamelled with a specific insulation thickness (t_i). Thus the distance between the two adjacent strands (p_{str}) can be found as (50). The alternative way to find the effective p_{str} is from the fill-factor of Litz wire (k_{fill}). For the given application, k_{fill} of profiled Litz wire is typically $(0.4\sim0.5)$ and p_{str} can be found as (51).

$$p_{str} = d_{str} + 2t_i \tag{50}$$

$$p_{str} = d_{str}\sqrt{\frac{\pi}{4k_{fill}}} \tag{51}$$

The height of the winding is given as,

$$h_{wdg} = h_2 - 2t_b \tag{52}$$

Where, (t_b) is the insulation thickness between core and winding. Furthermore, to find the width of the winding, first the effective number of layers (p) of the Litz wire is needed, which is also required for calculating the AC resistance of winding given in (36). It can be found by the following equation.

$$p_{pri} = N_P N_{str}\frac{p_{str}}{h_{wdg}} \;\; ; \;\; p_{sec} = N_S N_{str}\frac{p_{str}}{h_{wdg}} \tag{53}$$

p_{pri}/p_{sec} is the effective number of layers in the primary/secondary winding, where p_{pri} and p_{sec} are equal in this work due to the specified 1:1 turn ratio. Thus the width of the primary, as well as the secondary winding, can be found as,

$$w_{pri} = w_{sec} = p_{pri}p_{str} \tag{54}$$

From this radius r_3 and r_4 of the RT can be found as,

$$r_3 = w_{pri} + w_{sec} + w_s + 2t_b \tag{55}$$

$$r_4 = \sqrt{\left(\frac{A_c}{\pi} + r_3^2\right)} \tag{56}$$

This completes all of the dimensions required for the design of RT. Furthermore, the core loss given by (34) can then be assessed.

Step 2. Electric circuit parameters calculation: Once the geometry has been defined, (31) and (32) can be used to obtain all the parameters shown in Fig. 6, including the respective magnetising and leakage inductances. This step is required for the evaluation of converter performance in the next stage.

Step 3. Converter parameters calculation: Winding loss is calculated at this stage, based on RMS currents and effective AC resistance of both primary and secondary windings. Since the inductance values are known at this stage, the DAB control phase-shift angle can be obtained by (41) and then the RMS value of current by (42). Equation (36) gives the effective AC resistance. Finally, equation (37) is used to determine the winding loss.

Step 4. Thermal calculation: The insulation in the winding has a specific temperature tolerance, whereas the magnetic core is restricted by the curie temperature. Because the winding and core loss cause temperature rise, it is critical to predicting temperature distribution within RT, which is obtained by incorporating the thermal model discussed in Section II-C.

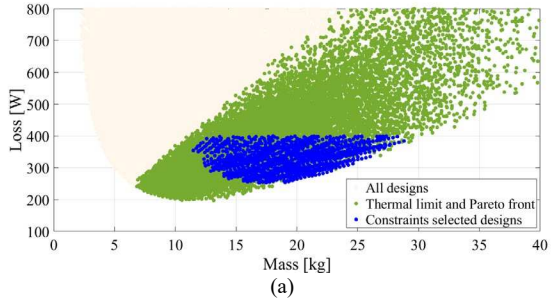

(a)

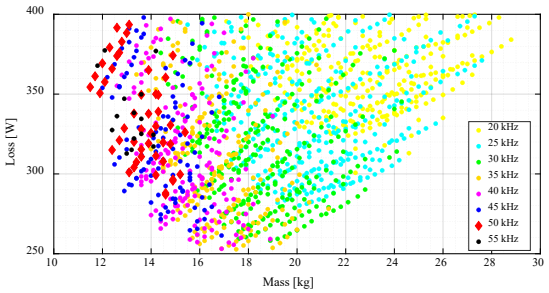

(b)

Fig. 11. Loss vs. mass of all possible RT designs for specifications listed in Table I, (a) including thermal limitations, design constraints and the filtered optimally chosen designs, and (b) the zoomed representation of constraints selected designs with various switching frequencies.

C. Constraints

It is important to identify practical constraints that might limit the number of initially obtained feasible RT design candidates. The primary design constraints for transformers are temperature rise and core saturation. Other factors to consider include operating frequency, volume, mass, minimal core thickness (due to possible manufacturing limits), control phase shift angle, etc. Taking into account identified system constraints, unpractical designs are filtered out and a new subset of practical design solutions is formed.

D. Objective function and optimal solution

The final stage of the optimization process includes the selection of the best design(s) among all practical design candidates based on the application-specific objective function. The optimization in this work is done in terms of minimal total mass and loss of RT.

E. Discussion

Fig. 11 depicts all feasible RT design candidates for the specifications given in Tables I and II, represented in terms of overall loss and mass. The bottom border is the Pareto front, which presents the trade-off between loss and mass. Further, simple post-processing reveals complicated design trends involving different system parameters, such as operating frequency, the number of turns and space envelope constraints. Fig. 12a and 12b show the variation of the minimum mass with the frequency and number of turns, where the required loss for minimum mass is found to be higher than the minimum possible loss. Thus, an optimal frequency and number of turns that minimises overall system mass do not

necessarily lead to minimum transformer loss. The feasibility constraint, which is governed by the practically achievable core thickness limits operating frequency above 55 kHz. Fig. 13 depicts the relationship between the core thickness and minimum mass, which, once again, does not provide minimum loss at the same time.

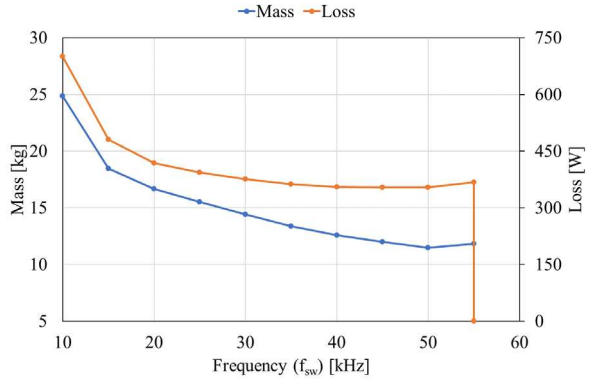

(a)

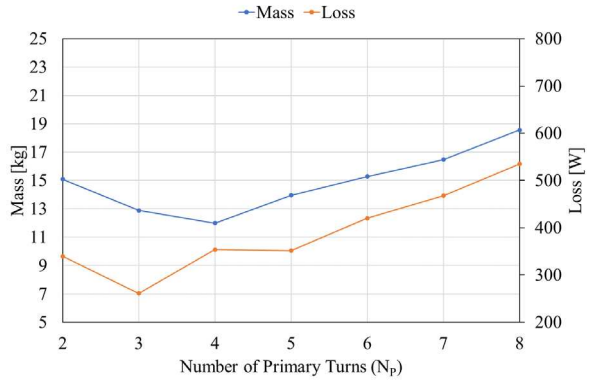

(b)

Fig. 12. Trends for achieving minimum mass with (a) frequency and (b) number of turns.

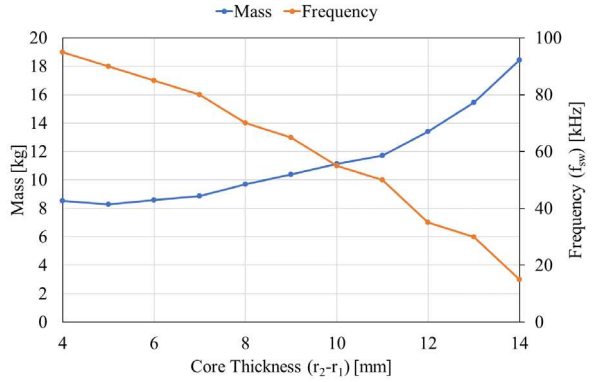

Fig. 13. Minimum mass possible for a given core thickness and optimal frequency.

IV. Conclusion

This paper proposes a general methodology for the optimal design of DAB-based radial-type RT; in that, it identifies critical optimization variables and analytically models the magnetic, electrical and thermal properties of RT. Further, a new analytical model of leakage inductance is developed and compared with the existing approximate solution in the literature. It develops a design optimization tool that requires basic system parameters, such as power, voltage and a space envelope, as inputs, based on which all feasible RT design candidates are generated while considering realistic system constraints, such as thermal limitations. Finally, the best solution(s) are selected based on the application-specific objective function.

References

[1] R. Manko, S. Corovic, and D. Miljavec, "Analysis and design of rotary transformer for wireless power transmission," in *Proc. IEEE Problems of Automated Electrodrive. Theory and Practice (PAEP)*, Kremenchuk, Ukraine, 2020, pp. 1–6.

[2] R. Chacko, M. H. Ravichandran, M. K. Sanoop, T. Sabu, V. T. Sadasivan Achari, and C. C. Joseph, "Magnetic slip ring-rotary transformer based novel non-contact signal transfer mechanism for spacecraft application," in *Proc. Annual International Conference on Emerging Research Areas: Magnetics, Machines and Drives (AICERA/iCMMD),* Kottayam, India, 2014, pp. 1–5.

[3] Enzo Michele Illiano. "Design of a highly efficient brushless current excited synchronous motor for automotive purposes,". PhD dissertation. Dept. Mech. Process Eng., ETH-Zürich, Zürich, 2014.

[4] J.P.C. Smeets et al. "Optimal design of a pot core rotating transformer,". in *Proc. IEEE Energy Conversion Congress and Exposition (ECCE),* Atlanta, GA, USA, 2010, pp. 4390–4397.

[5] T. Raminosoa, R. H. Wiles and J. Wilkins, "Novel rotary transformer topology with improved power transfer capability for high-speed applications," *IEEE Trans. Ind. Appl.*, vol. 56, no. 1, pp. 277-286, Jan.-Feb. 2020.

[6] J. Legranger, G. Friedrich, S. Vivier and J. C. Mipo, "Comparison of two optimal rotary transformer designs for highly constrained applications," in *Proc. IEEE International Electric Machines & Drives Conference (IEMDC)*, Antalya, Turkey, 2007, pp. 1546-1551.

[7] K. Bastiaens, D. C. J. Krop, S. Jumayev and E. A. Lomonova, "Design and comparison of high-frequency resonant and non-resonant rotating transformers," *in Proc. 21st International Conference on Electrical Machines and Systems (ICEMS)*, Shenzen, China, 2018, pp. 1703-1708.

[8] Muhlethaler, J. and Kolar, J. W. and Ecklebe, A, "A novel approach for 3d air gap reluctance calculations," *8th International Conference on Power Electronics - ECCE Asia*, 2011, pp. 446-452.

[9] K. Venkatachalam *et al*. "Accurate prediction of ferrite core loss with nonsinusoidal waveforms using only Steinmetz parameters,". in *Proc. IEEE Workshop on Computers in Power Electronics (COMPEL)*, Aalborg, Denmark, 2002, pp. 36–41.

[10] Qingchao Meng and Jürgen Biela. "Survey and comparison of 1D/2D analytical models of HF losses in litz wire,". In *Proc. 22nd European Conference on Power Electronics and Applications (EPE'20 ECCE Europe)*, Lyon, France. 2020, p.1–p.11.

[11] D. Das and K. Basu, ``Optimal Design of a Dual-Active-Bridge DC-DC Converter," *IEEE Transactions on Industrial Electronics*, vol. 68, no. 12, pp. 12034-12045, Dec. 2021.